

Constraining neutrino electromagnetic properties by germanium detectors

Jiunn-Wei Chen,^{1,2,*} Hsin-Chang Chi,^{3,†} Keh-Ning Huang,^{1,4,5} Hau-Bin Li,⁶ C.-P. Liu,^{3,‡} Lakhwinder Singh,^{6,7} Henry T. Wong,⁶ Chih-Liang Wu,^{1,6} and Chih-Pan Wu¹

¹*Department of Physics, National Taiwan University, Taipei 10617, Taiwan*

²*National Center for Theoretical Sciences and Leung
Center for Cosmology and Particle Astrophysics,
National Taiwan University, Taipei 10617, Taiwan*

³*Department of Physics, National Dong Hwa University, Shoufeng, Hualien 97401, Taiwan*

⁴*Department of Physics, Sichuan University, Chengdu, Sichuan, China*

⁵*Department of Physics, Fuzhou University, Fuzhou, Fujian, China*

⁶*Institute of Physics, Academia Sinica, Taipei 11529, Taiwan*

⁷*Department of Physics, Banaras Hindu University, Varanasi 221005, India*

Abstract

The electromagnetic properties of neutrinos, which are either trivial or negligible in the context of the Standard Model, can probe new physics and have significant implications in astrophysics and cosmology. The current best direct limits on the neutrino millicharges and magnetic moments are both derived from data taken with germanium detectors with low thresholds at keV levels. In this paper, we discuss in detail a robust, *ab initio* method: the multiconfiguration relativistic random phase approximation, that enables us to reliably understand the germanium detector response at the sub-keV level, where atomic many-body physics matters. Using existing data with sub-keV thresholds, limits on reactor antineutrino's millicharge, magnetic moment, and charge radius squared are derived. The projected sensitivities for next generation experiments are also given and discussed.

* jwc@phys.ntu.edu.tw

† hsinchang@mail.ndhu.edu.tw

‡ cpliu@mail.ndhu.edu.tw

I. INTRODUCTION

Investigations of neutrino properties continue to be an accretive field of emerging interests to both theoretical and experimental physicists. Their nonzero masses, as suggested by neutrino oscillation experiments with various sources, already hint the necessity of extending the Standard Model (SM) to accommodate massive neutrinos. It is no wonder that their properties such as absolute masses, mass hierarchy, Dirac or Majorana nature, and precise mixing parameters are among the most actively pursued topics in neutrino physics for their great discovery potential.

Another interesting venue to look for surprises in neutrinos is their nontrivial electromagnetic (EM) properties (see, e.g., [1] for recent reviews). In the SM, neutrinos are strictly neutral. Their tiny charge radii squared, magnetic dipole moments, anapole moments (require parity violation in addition), and electric dipole moments (require both parity and time-reversal violation in addition) only arise in forms of radiative corrections (in some cases, finite mass terms and flavor mixing matrix have to be included). Going beyond the SM, there are numerous conjectures of larger neutrino EM moments, including neutrinos being millicharged. The present best upper limits on some of these moments, either set directly by experiments, or inferred indirectly from observational evidences combined with theoretical arguments, are orders of magnitude larger than the SM predictions (see [2] and references therein for the current status). As a result, this leaves space for new physics. Also, the additional EM interactions with the copious amount of neutrinos in the universe will have significant implications for astrophysics and cosmology.

It was recently identified [3, 4] that the unexplored interaction channel of neutrino-induced atomic ionization:

$$\nu + A \rightarrow \nu + A^- + e^- ,$$

is an interesting avenue to study possible neutrino electromagnetic effects, and has the potentials of producing surprises. The germanium atom (Ge) is selected for the studies, since there are matured Ge detector techniques with low (at the atomic transition range of keV) threshold and good resolution to resolve possible spectra structures and peaks and endpoints, which are essential to provide smoking-gun positive signatures. Existing data from the TEXONO and GEMMA experiments with reactor neutrinos already provide bounds on neutrino magnetic moments [5-8], neutrino charge radius [9], and milli-charges [10, 11]. New

generations of Ge detectors capable of measuring events as low as 100 eV are expected to further expand the sensitivities [12–15].

To interpret experimental data and put limits on these moments, an important theoretical input: the differential cross section formulae for neutrino scattering in detectors, is necessary (see, e.g., Ref. [16] for a recent review of neutrino-atom collision theory). While the conventional approach of treating the atomic electrons as free particles is considered a good approximation at high energies, at sub-keV regime, which is similar to atomic scales, proper treatments of many-electron dynamics in atomic ionization must be incorporated for a better understanding of detector responses at low energies.

Motivated by this goal, we recently applied *ab initio* calculations in the framework of multiconfiguration relativistic random phase approximation (MCR-RPA) theory to study the atomic ionization of germanium by neutrino scattering. Partial results were reported in [17] and [4], which dealt with the neutrino magnetic moment and millicharge, respectively.

The purpose of this article is twofold: On the theory part, we present our approach in full details, elaborate in particular the benchmark calculations that serve as a concrete basis on which the method and uncertainty estimate can be justified, and consider all observables that can be probed by atomic ionization. Comparisons with previous works [3, 18–24] are given so that differences in various approaches and the applicability of various approximation schemes at the sub-keV regime can be clearly examined.

The organization of this paper is as follows. In Section II, we give the general formulation of atomic ionization by neutrinos, and mention two widely-used approximation schemes: free electron approximation and equivalent photon approximation in II A and II B, respectively. Our approach to atomic many-body problems: the multiconfiguration relativistic random phase approximation, is outlined in Section III A, and its application to the structure and photoionization of germanium atoms are described in Section III B and III C, subsequently. In Section IV A, we present and discuss our results for germanium ionization by neutrino scattering, and compare with existing works. Limits on neutrino electromagnetic moments are derived in Section IV B by using realistic reactor antineutrino spectra and data. As there have been proposals of using neutrinos from tritium β decay to study neutrino magnetic moment [21, 25, 26], our calculation for this case is presented in Section IV C. The summary is in Section V, and the technical details of multipole expansion, which is relevant to our calculations, is in Appendix I.

II. FORMULATION OF ATOMIC IONIZATION BY NEUTRINOS

Consider the ionization of an atom A by scattering a neutrino ν_l (l denoting the flavor eigenstate) off atomic bound electrons

$$\nu_l + A \rightarrow \nu_l + A^+ + e^- . \quad (1)$$

For $l = \mu, \tau$, the process only proceeds through the neutral weak interaction (in t -channel), while for $l = e$, the charged weak interaction (in s -channel) also contributes. Using a Feirz reordering, the general low-energy weak scattering amplitude can be compactly gathered in one formula

$$\mathcal{M}^{(w)} = \frac{G_F}{\sqrt{2}} j_\mu^{(w)} (c_V \mathcal{J}^\mu - c_A \mathcal{J}_5^\mu) , \quad (2)$$

where G_F is the Fermi constant. The neutrino weak current

$$j_\mu^{(w)} = \bar{\nu}(k_2, s_2) \gamma_\mu (1 - \gamma_5) \nu(k_1, s_1) , \quad (3)$$

takes on the usual Dirac bilinear form with $k_1 = (\omega_1, \vec{k}_1)$, $k_2 = (\omega_2, \vec{k}_2)$ being the four-momenta and s_1, s_2 being the helicity states of the neutrino before and after scattering, respectively. The energy and 3-momentum transfer by the neutrinos are defined as

$$q^\mu = (T, \vec{q}) = (\omega_1 - \omega_2, \vec{k}_1 - \vec{k}_2) . \quad (4)$$

The atomic (axial-)vector current, $\mathcal{J}_{(5)}^\mu$,

$$\mathcal{J}_{(5)}^\mu \equiv \langle \Psi_f | \hat{\mathcal{J}}_{(5)}^\mu(-\vec{q}) | \Psi_i \rangle = \int d^3x e^{i\vec{q}\cdot\vec{x}} \langle \Psi_f | \hat{\psi}_e(\vec{x}) \gamma^\mu (\gamma_5) \hat{\psi}_e(\vec{x}) | \Psi_i \rangle , \quad (5)$$

is the matrix element of a one-electron (axial-)vector current operator $\hat{\mathcal{J}}_{(5)}^\mu(-\vec{q})$ (in momentum space) evaluated with many-body atomic initial and final states, $|\Psi_i\rangle$ and $|\Psi_f\rangle$. The vector and axial-vector coupling constants are

$$c_V = -\frac{1}{2} + 2 \sin^2 \theta_w + \delta_{l,e} , \quad c_A = -\frac{1}{2} + \delta_{l,e} , \quad (6)$$

where θ_w is the Weinberg angle. The extra Kronecker delta is added to account for the additional s -channel scattering for ν_e .

Now suppose a neutrino has nonzero electromagnetic (EM) moments; in the most general case, the associated EM current can be expressed as

$$j_\mu^{(\gamma)} = \bar{\nu}(k_2, s_2) \left[F_1(q^2) \gamma_\mu - i(F_2(q^2) + iF_E(q^2) \gamma_5) \sigma_{\mu\nu} q^\nu + F_A(q^2) (q^2 \gamma_\mu - \not{q} q_\mu) \gamma_5 \right] \nu(k_1, s_1) \quad (7)$$

where $q^2 \equiv q_\mu q^\mu$. The four terms $F_1(q^2)$, $F_2(q^2)$, $F_A(q^2)$, and $F_E(q^2)$ are referred as the charge, anomalous magnetic, anapole, and electric dipole form factors, respectively. Up to the order of q^2 in $j_\mu^{(\gamma)}$, we define the electric charge, charge radius squared, magnetic dipole moment, anapole moment, and electric dipole moment of a neutrino by

$$\begin{aligned}
q_\nu &= F_1(0), \\
\langle r_\nu^2 \rangle &= 6 \frac{d}{dq^2} F_1(q^2) \Big|_{q^2 \rightarrow 0}, \\
\kappa_\nu &= F_2(0), \\
a_\nu &= F_A(0), \\
d_\nu &= F_E(0),
\end{aligned} \tag{8}$$

respectively, and they are all measured in the fundamental charge units e . Note that the existence of a_ν violates parity conservation, and d_ν violates both parity and time-reversal conservation. Also, in the Standard Model, the values of both $\langle r_\nu^2 \rangle$ and a_ν arising from electroweak radiative corrections are not gauge-independent quantities; only after the full radiative corrections being considered are the gauge-independent, physical observables resulted in [27]. While there are attempts to define these moments in gauge-independent manners, but still controversial. Here we do not concern ourselves further with such subtleties, but just practically assume these exotic moments, whose definitions are consistent with current conservation as obviously seen in Eq. (7), exist, and study their contributions in scattering processes.

Any nonzero EM moments of a neutrino therefore generate additional contributions to the atomic ionization process; they are given by the associated EM scattering amplitude ¹

$$\mathcal{M}^{(\gamma)} = \frac{4\pi\alpha}{q^2} j_\mu^{(\gamma)} \mathcal{J}^\mu. \tag{9}$$

Before presenting the complete scattering formula, we discuss a few kinematical considerations that help to reduce the full result to a simpler form.

First, as neutrinos are much lighter than all the energy scales relevant to the atomic ionization processes of concern, an ultrarelativistic limit $m_\nu \rightarrow 0$ is considered a good approximation. In such cases, the chirality and helicity states of a neutrino are the same, so

¹ We note that a non-zero q_ν also induces extra neutral weak interactions which modify Eq. 2 at the order of $q_\nu \sin^2 \theta_w$; therefore can be safely ignored.

scattering amplitudes of neutrino-helicity-flipping interactions with κ_ν and d_ν , do not interfere with ones of neutrino-helicity-conserving interactions. On the other hand, since weak interactions and those with \mathfrak{q}_ν , $\langle \mathfrak{r}_\nu^2 \rangle$, and \mathfrak{a}_ν all preserve helicity, there are interference terms between the weak and EM amplitudes. Their magnitudes are important when constraints of \mathfrak{q}_ν , $\langle \mathfrak{r}_\nu^2 \rangle$, and \mathfrak{a}_ν are to be extracted from experimental data.

Second, the interaction with $\langle \mathfrak{r}_\nu^2 \rangle$ apparently takes a four-Fermi contact form (evidenced by the $1/q^2$ photon propagator being cancelled by the q^2 factor in the associated current), and so does the interaction with \mathfrak{a}_ν [27]. As a result, the combined EM scattering amplitude

$$\mathcal{M}^{\langle \mathfrak{r}_\nu^2 \rangle + \mathfrak{a}_\nu} = 4\pi\alpha[\bar{\nu}\gamma_\mu(1/6\langle \mathfrak{r}_\nu^2 \rangle + \mathfrak{a}_\nu\gamma_5)\nu]\mathcal{J}^\mu, \quad (10)$$

look similar to $\mathcal{M}^{(w)}$, except no coupling to the atomic axial-vector current \mathcal{J}_5^μ .

Third, by the identities

$$\bar{\nu}_L\gamma_\mu\nu_L = -\bar{\nu}_L\gamma_\mu\gamma_5\nu_L, \quad \bar{\nu}_R\sigma_{\mu\nu}\nu_L = -\bar{\nu}_R\sigma_{\mu\nu}\gamma_5\nu_L, \quad (11)$$

one deduces that $\langle \gamma_\nu^2 \rangle$ and a_ν can not be distinguished in ultrarelativistic neutrino scattering and should effectively appear as one moment, the effective charge radius squared:

$$\langle \mathfrak{r}_\nu^2 \rangle^{(\text{eff})} = \langle \mathfrak{r}_\nu^2 \rangle - 6\mathfrak{a}_\nu. \quad (12)$$

The same argument applies to κ_ν and d_ν that they appear as one effective anomalous magnetic moment:

$$\kappa_\nu^{(\text{eff})} = \kappa_\nu - id_\nu. \quad (13)$$

Starting from the total scattering amplitude, $\mathcal{M}^{(w)} + \mathcal{M}^{(\gamma)}$, and following the standard procedure, the single differential cross section with respect to neutrino energy deposit T for an inclusive process with a unpolarized target is obtained. When there is only weak scattering, the result is

$$\begin{aligned} \frac{d\sigma^{(w)}}{dT} = & \frac{G_F^2}{\pi}(E_\nu - T)^2 \int d\cos\theta \cos^2\frac{\theta}{2} \left\{ R_{00}^{(w)} - \frac{T}{|\vec{q}|} R_{03+30}^{(w)} + \frac{T^2}{|\vec{q}|^2} R_{33}^{(w)} \right. \\ & \left. + \left(\tan^2\frac{\theta}{2} - \frac{q^2}{2|\vec{q}|^2} \right) R_{11+22}^{(w)} + \tan\frac{\theta}{2} \sqrt{\tan^2\frac{\theta}{2} - \frac{q^2}{|\vec{q}|^2}} R_{12+21}^{(w)} \right\} \end{aligned} \quad (14)$$

where θ is the neutrino scattering angle, E_ν is the incident neutrino energy. The atomic weak response functions

$$\begin{aligned} R_{\mu\nu}^{(w)} = & \frac{1}{2J_i + 1} \sum_{M_{J_i}} \sum_f \langle \Psi_f | c_V \hat{\mathcal{J}}_\mu - c_A \hat{\mathcal{J}}_{5\mu} | \Psi_i \rangle \langle \Psi_f | c_V \hat{\mathcal{J}}_\nu - c_A \hat{\mathcal{J}}_{5\nu} | \Psi_i \rangle^* \\ & \times \delta(T + E_i - E_f), \end{aligned} \quad (15)$$

involve a sum of the final scattering states $|\Psi_f\rangle$ and a spin average of the initial states $|\Psi_i\rangle = |J_i, M_{J_i}, \dots\rangle$, and the Dirac delta function imposes energy conservation. The Greek indices μ, ν take values 0, 1, 2, 3, and without loss of generality, the direction of \vec{q} is taken to be the quantization axis with $\mu = 3$.

The contributions from the helicity-conserving (h.c.) interactions with \mathfrak{q}_ν and $\langle \mathfrak{r}_\nu \rangle^{(\text{eff})}$, as they interfere with the weak scattering, can be compactly included by the following substitution

$$\frac{d\sigma^{(w)}}{dT} \rightarrow \frac{d\sigma^{(\text{h.c.})}}{dT}, \quad \text{with } c_V \rightarrow c_V + 2\sqrt{2}\pi \frac{\alpha}{G_F} \left(\frac{1}{q^2} \mathfrak{q}_\nu^2 + \frac{1}{6} \langle \mathfrak{r}_\nu^2 \rangle^{(\text{eff})} \right). \quad (16)$$

It should be pointed out that the inclusion of \mathfrak{q}_ν is only formally, as it goes with a kinematics-dependent term $1/q^2$ that differentiates its contribution from the other contact interactions.

As will be explicitly shown later, the contribution from \mathfrak{q}_ν with the current upper limit $\lesssim 10^{-12}$ derived from direct measurements dominates over the weak scattering. When the \mathfrak{q}_ν -weak interference terms are much less important, it is convenient to isolate the pure Coulomb (coul) scattering part,

$$\begin{aligned} \frac{d\sigma^{(\text{coul})}}{dT} &= \mathfrak{q}_\nu^2 (2\pi\alpha^2) \left(1 - \frac{T}{E_\nu} \right) \int d\cos\theta \left\{ \frac{(2E_\nu - T)^2 - |\vec{q}|^2}{|\vec{q}|^4} R_{00}^{(\gamma)} \right. \\ &\quad \left. - \left[\frac{q^2 + 4E_\nu(E_\nu - T)}{2|\vec{q}|^2 q^2} + \frac{1}{q^2} \right] R_{11+22}^{(\gamma)} \right\}, \end{aligned} \quad (17)$$

which is proportional to \mathfrak{q}_ν^2 . In such cases, we apply the approximated form

$$\left. \frac{d\sigma^{(\text{h.c.})}}{dT} \right|_{\text{large } \mathfrak{q}_\nu} \approx \left. \frac{d\sigma^{(\text{h.c.})}}{dT} \right|_{c_V \rightarrow c_V + \frac{\sqrt{2}\pi\alpha}{3G_F} \langle \mathfrak{r}_\nu^2 \rangle^{(\text{eff})}} + \frac{d\sigma^{(\text{coul})}}{dT}. \quad (18)$$

On the other hand, the contribution from the the helicity-violating (h.v.) interaction with $\mathfrak{k}_\nu^{(\text{eff})}$ has no interference with the helicity-conserving part so that

$$\frac{d\sigma}{dT} = \frac{d\sigma^{(\text{h.c.})}}{dT} + \frac{d\sigma^{(\text{h.v.})}}{dT}, \quad (19)$$

with

$$\begin{aligned} \frac{d\sigma^{(\text{h.v.})}}{dT} &= (\mathfrak{k}_\nu^2 + \mathfrak{d}_\nu^2) (2\pi\alpha^2) \left(1 - \frac{T}{E_\nu} \right) \int d\cos\theta \left\{ - \frac{(2E_\nu - T)^2 q^2}{|\vec{q}|^4} R_{00}^{(\gamma)} \right. \\ &\quad \left. + \frac{q^2 + 4E_\nu(E_\nu - T)}{2|\vec{q}|^2} R_{11+22}^{(\gamma)} \right\}. \end{aligned} \quad (20)$$

Note that the EM response functions appearing in Eqs. (17) and (20) are related to the weak response functions by setting $c_V = 1$ and $c_A = 0$ in Eq. (15)

$$R_{\mu\nu}^{(w)}|_{c_V=1, c_A=0} \rightarrow R_{\mu\nu}^{(\gamma)}, \quad (21)$$

as EM interactions only couple to vector currents (which result in $R_{12+21}^{(\gamma)} = 0$). Because of vector current conservation, the longitudinal part of a spatial current density ($\mu = 3$) is related to the charge density ($\mu = 0$). Therefore the response functions $R_{03+30}^{(\gamma)}$ and $R_{33}^{(\gamma)}$ are subsumed in $R_{00}^{(\gamma)}$.

A couple of important remarks on kinematics in $d\sigma/dT$ are due here: (i) For fixed E_ν and T , the square of four momentum transfer q^2 in the ultrarelativistic limit is determined by the neutrino scattering angle θ

$$q^2 = -4E_\nu^2 \sin^2\left(\frac{\theta}{2}\right) - m_\nu^2 \frac{T^2}{E_\nu^2}. \quad (22)$$

It will not vanish even at the forward angle $\theta = 0$ as long as the neutrino is not massless $m_\nu \neq 0$. (This is important for scattering with \mathfrak{q}_ν). (ii) By four momentum conservation, the integration variable $\cos\theta$ is constrained by

$$\min \left\{ 1, \max \left[-1, \frac{E_\nu^2 + (E_\nu - T)^2 - 2M_A(T - B)}{2E_\nu(E_\nu - T)} \right] \right\} \leq \cos\theta \leq 1, \quad (23)$$

where M_A is the atomic mass and B is the binding energy of the ejected electron.

To evaluate $d\sigma/dT$, the most challenging task is the calculation of all relevant atomic response functions, Eqs.(15,21). Before discussing our *ab initio* approach in next section, we review a couple of simple approximation schemes that work in certain kinematic regimes and by which tedious many-body calculations can be spared.

A. Free Electron Approximation

In case of high energy scattering when electron binding energy is comparatively negligible, a conceptually straightforward approach is to use a neutrino-free-electron scattering formula $d\sigma^{(0)}/dT$. The number of atomic electrons can be freed depends on the neutrino energy deposition T . By introducing a step function $\theta(T - B_i)$ to judge whether the i th electron, with binding energy B_i , can contribute to the scattering process, one obtains the conventional scattering formula based on the free electron approximation

$$\left. \frac{d\sigma}{dT} \right|_{\text{FEA}} = \sum_{i=1}^Z \theta(T - B_i) \left. \frac{d\sigma^{(0)}}{dT} \right|_{q^2 = -2m_e T}. \quad (24)$$

Despite FEA enjoys a lot of success in many situations, its applicability is not always self-evident, in particular when issues like relevant energy scales and kinematics of concern arise. For example, as it was shown explicitly in Ref. for hydrogen-like atoms: (i) The borderline incident neutrino energy above which FEA can apply is the binding momentum $\sim Zm_e\alpha$, instead of the binding energy $\sim Z^2m_e\alpha^2$. (ii) Because FEA only has a specific $q^2 = -2m_eT$ in contrary to an allowed range prescribed by Eqs. (22,23) for the realistic case, it fails to be valid for relativistic muon scattering and nonrelativistic WIMP scattering. Therefore, to reduce the potential errors caused this conventional practice in particular for detector's response at low energies is an important theoretical task.

B. Equivalent Photon Approximation

In typical EM scattering with ultrarelativistic charged particles, it was long established that the equivalent photon approximation (EPA) is well founded [28–30]. Such processes mostly happen with peripheral scattering angles, i.e., $q^2 \rightarrow 0$; it is thus obvious from Eq. (17) that the contribution from the transverse response function $R_{11+22}^{(\gamma)}$ dominates and the longitudinal part $R_{00}^{(\gamma)}$ can be ignored. As the “on-shell” transverse response function is directly linked to the total cross section of photoabsorption

$$\sigma_{\text{abs}}^{(\gamma)}(T) = \frac{2\pi^2\alpha}{T} R_{11+22}^{(\gamma)}(q^2 = 0), \quad (25)$$

the EPA further approximates $R_{11+22}^{(\gamma)}(q^2) \approx R_{11+22}^{(\gamma)}(0)$ so that the Coulomb differential cross section for \mathfrak{d}_ν

$$\left. \frac{d\sigma^{(\text{coul})}}{dT} \right|_{\text{EPA}} = -\mathfrak{d}_\nu^2 \left(\frac{\alpha}{\pi} \right) \left(1 - \frac{T}{E_\nu} \right) \sigma_{\text{abs}}^{(\gamma)}(T) \int d\cos\theta \left[\frac{q^2 + 4E_\nu(E_\nu - T)}{2|\vec{q}|^2 q^2} + \frac{1}{q^2} \right], \quad (26)$$

can be directly determined by experiment.

Applying similar procedure to EM scattering with κ_ν and \mathfrak{d}_ν :

$$\left. \frac{d\sigma^{(\text{h.v.})}}{dT} \right|_{\text{EPA}} = (\kappa_\nu^2 + \mathfrak{d}_\nu^2) \left(\frac{\alpha}{\pi} \right) \left(1 - \frac{T}{E_\nu} \right) \sigma_{\text{abs}}^{(\gamma)}(T) \int d\cos\theta \left[\frac{q^2 + 4E_\nu(E_\nu - T)}{2|\vec{q}|^2} \right], \quad (27)$$

the cross section formula differs noticeably from the previous case by missing of the $1/q^2$ enhancement in the real photon limit. For more discussions about why there should not be atomic-enhanced sensitivities to neutrino magnetic moments at low energies, in contrary to what was claimed in Ref. [3] (which is based on a slight different twist of Eq. 27), we refer readers to Refs. [22, 31] for details.

III. *AB INITIO* DESCRIPTION OF GERMANIUM

To go beyond the simple approximation schemes mentioned in the last section and evaluate the cross section formulae more reliably at low energies, the structure and ionization of detector atoms have to be considered on a more elaborate basis. In this section, we first introduce our approach to the atomic many-body problems: the multiconfiguration relativistic random phase approximation (MCRRPA) theory. In the following subsections, we present our results for the structure and photoionization of germanium atoms, respectively, and benchmark the quality of MCRRPA as reliable approach to describe the responses of germanium detectors.

A. The MCRRPA Theory

The relativistic random-phase approximation (RRPA) has been applied, with remarkable successes, to photoexcitation and photoionization of closed-shell atoms and ions of high nuclear charge, such as heavy noble gas atoms, where the ground state is well isolated from the excited states. For other closed-shell systems, such as alkaline-earth atoms, which have low-lying excited states, such applications have been less successful, owing to the importance of two-electron excitations which are omitted in the RRPA. The MCRRPA theory is a generalization RRPA by using a multiconfiguration wave function as the reference state which is suitable for treating photoexcitation and photoionization of closed-shell and certain open-shell systems of high nuclear charge. The great success it achieved in various atomic radiative processes can be found in Refs. [32]. A detailed formulation of the MCRRPA has been given in a previous paper [33], and we summarize the essential features here.

One way to derive the MCRRPA equations is through linearizing the time-dependent

multiconfiguration Hartree-Fock (TDHF) equations.² For a N -electron atomic system, the time-dependent relativistic Hamiltonian is given by

$$H(t) = H_0 + V(t), \quad (28)$$

where the unperturbed Hamiltonian

$$H_0 = \sum_{i=1}^N h(\vec{r}_i) + \sum_{i<j}^N \frac{e^2}{r_{ij}}, \quad (29)$$

contains the sum of single-electron Dirac Hamiltonians

$$h(\vec{r}) = c\vec{\alpha} \cdot \vec{p} + \beta c^2 - \frac{Z}{r}, \quad (30)$$

and the Coulomb repulsion between two-electron pairs (the latter summation); and the time-dependent external perturbation

$$V(t) = \sum_{i=1}^N v_+(\vec{r}_i) e^{-i\omega t} + \sum_{i=1}^N v_-(\vec{r}_i) e^{+i\omega t}, \quad (31)$$

takes a harmonic form and induces transitions between atomic states. Note that atomic units (a.u.) are employed throughout this paper.

Let $\Phi(t)$ be the time-dependent solution of the wave equation

$$i \frac{\partial \Phi(t)}{\partial t} = H(t) \Phi(t), \quad (32)$$

our point of departure to obtaining $\Phi(t)$ is through the time-dependent variational principle

$$\left\langle \delta \Phi(t) \left| \left[i \frac{\partial}{\partial t} - H(t) \right] \right| \Phi(t) \right\rangle = 0. \quad (33)$$

Without loss of generality, it is convenient to factor out from $\Phi(t)$ the phase due to the time-evolution of the stationary state of H_0

$$\Phi(t) = e^{-iEt} \Psi(t), \quad (34)$$

with E denoting the energy eigenvalue of H_0 . As a result, the time-dependent variational principle is recast as

$$\left\langle \delta \Psi(t) \left| \left[E + i \frac{\partial}{\partial t} - H(t) \right] \right| \Psi(t) \right\rangle = 0. \quad (35)$$

² An alternatively derivation from an equation-of-motion point of view is given in Ref. [34].

For an atomic state with angular momentum JM and parity π , the multiconfiguration Hartree-Fock approximation assumes the wave function $\Psi(t)$ as a superposition of configuration wave functions $\psi_a(t)$ of the same JM and π , viz.

$$\Psi(t) = \sum_a C_a(t) \psi_a(t), \quad (36)$$

where a is a configuration index, and $C_a(t)$ are time-dependent weights. The configuration wave functions $\psi_a(t)$ are built up from one-electron orbitals $u_\alpha(t)$. To guarantee the normalization of $\Psi(t)$

$$\langle \Psi(t) | \Psi(t) \rangle = 1, \quad (37)$$

the following subsidiary conditions

$$\langle u_\alpha(t) | u_\beta(t) \rangle = \delta_{\alpha\beta}, \quad (38)$$

$$\langle \psi_a(t) | \psi_b(t) \rangle = \delta_{ab}, \quad (39)$$

$$\sum_a C_a^*(t) C_a(t) = 1, \quad (40)$$

are imposed. Since the perturbation $V(t)$ that induces atomic transitions is harmonic in time, both $C_a(t)$ and $u_\alpha(t)$ assume the following expansion

$$C_a(t) = C_a + [C_a]_+ e^{-i\omega t} + [C_a]_- e^{+i\omega t} \dots, \quad (41)$$

$$u_\alpha(t) = u_\alpha + w_{\alpha+} e^{-i\omega t} + w_{\alpha-} e^{+i\omega t} + \dots, \quad (42)$$

where “...” denotes higher harmonic responses.

Approximate time-dependent solution of Eq. (35) are thus obtained with the wave function, Eq. (36), constrained by Eqs. (37–42). The terms C_a and u_α , which are independent of the external field, lead to the usual stationary multiconfiguration Dirac-Fock (MCDF) description of an atomic state and this gives the initial state wave function $|\Psi_i\rangle$ of our problem. The terms $[C_a]_\pm$ and $w_{\alpha\pm}$, which are induced by the external field, lead to equations describing the linear response of the atomic state to the external field; these linear response equations are called the multiconfiguration relativistic random-phase approximation (MCRRPA) equations [33, 35]. Furthermore, the incoming wave boundary condition is incorporated to yield the physical asymptotic Coulomb wave function that describes an

outgoing continuum electron with a residual ion in the final state $\langle \Psi_f |$ of our problem. Since the external perturbation $V(t)$ may have components with nonvanishing angular momentum and with odd parity, the atomic wave function contains terms of mixed angular momentum and parity. If one starts from a single-configuration reference state, the MRRPA equations reduce to the usual RPA equations.

To make connection with the general scattering formalism set up in the last section, we note that the perturbing field components v_{\pm} take the matrix form

$$\langle \Psi_f, E_f = E_i \pm \omega | v_{\pm}^{(w,\gamma)} | \Psi_i \rangle = \mathcal{M}^{(w,\gamma)} |_{E_f=E_i \pm \omega}, \quad (43)$$

and they cause atomic excitation and de-excitation by an energy quantum ω , respectively. Therefore, in the process of solving the MRRPA equations, the corresponding scattering amplitudes are simultaneously determined.

Another important point to mention in our implementation of the MRRPA scheme is the choice of the spherical-wave basis. As a result, all transition operators are cast into spherical multipole operators. The key step in the spherical multipole expansion is breaking down the atomic charge density operator $\hat{\mathcal{J}}^0(-\vec{q})$ into a series of charge multipole operators \hat{C}_{JM} , and the atomic 3-current density operator $\hat{\mathcal{J}}^i(-\vec{q})$ into a series of longitudinal \hat{L}_{JM} , transverse electric \hat{E}_{JM} , and transverse magnetic \hat{M}_{JM} multipole operators, with JM denoting the angular momentum quantum numbers. The advantages of such an implementation include: (i) The three-dimensional equation of motion for each orbital is reduced to a one-dimensional equation. (ii) Each multipole operator has its own angular momentum and parity selection rules, so the MRRPA equations can be divided into smaller blocks in which numerical calculations can be performed more efficiently. (iii) For $1/|\vec{q}|$ larger than the size of the atom, the multipole expansion converges rapidly. For the axial charge $\hat{\mathcal{J}}_5^0(-\vec{q})$ and 3-current $\hat{\mathcal{J}}_5^i(-\vec{q})$, four more types of multipole operators \hat{C}_{JM}^5 , \hat{L}_{JM}^5 , \hat{E}_{JM}^5 , and \hat{M}_{JM}^5 , are to be introduced. Each of them has opposite parity selection rule compared to its vector counterpart. The details of the multipole expansion is given in Appendix I.

B. Atomic Structure of Germanium by MCDF

For the germanium atom, we chose the multiconfiguration reference state to be

$$\Psi = C_1 (4p_{1/2}^2)_0 + C_2 (4p_{3/2}^2)_0, \quad (44)$$

a linear combination of two configurations with total angular momentum $J = 0$ and parity $\pi = \text{even}$, where the coefficients C_1 and C_2 are the configuration weights. The notation $(4l_j^2)$ denotes symbolically an anti-symmetrized wave function constructed from two electrons in the valence orbital $4l_j$. The rest of the electrons in the 10 inner orbitals $4s_{1/2}$, $3d_{5/2}$, $3d_{3/2}$, $3p_{3/2}$, $3p_{1/2}$, $3s_{1/2}$, $2p_{3/2}$, $2p_{1/2}$, $2s_{1/2}$, and $1s_{1/2}$ form the closed core.

The ground-state wave function obeying the MCDF equations is solved by the computer code [36], which yields all the core and valence orbitals, and the configuration weights C_1 and C_2 . In Table I, all calculated orbital binding energies are shown and compared with the edge energies extracted from photoabsorption data of germanium solids (to be discussed in the next section). In Table I, the configuration weights and their corresponding percentages are given.

C. Photoabsorption of Germanium by MRRPA

To further benchmark the MRRPA method, in particular its applicability to the atomic bound-to-free transition of germanium, we consider the photoabsorption of germanium above the ionization threshold, for which experimental data are available.

In the multipole expansion scheme, an external perturbing field with parameters J and λ gives rise to one-particle-one-hole excitation channels which are restricted by the angular momentum and parity conservation. Suppose one of the atomic bound electron in the nl_j orbital is promoted to a free continuum state $\epsilon l'_j$, (ϵ denotes the kinetic energy) by this $J\lambda$ perturbing field, the relevant quantum numbers then satisfy the following selection rules:

$$|j - J| \leq j' \leq |j + J|, \quad (\text{Angular Momentum Selection Rule}) \quad (45)$$

$$l + l' + J + \lambda - 1 = \text{even}. \quad (\text{Parity Selection Rule}) \quad (46)$$

As a result, in response to the multipole perturbations (with different $J\lambda$), the germanium atom (a many-body 1S_0 state) is excited to a state mixed with components of different total angular momenta and parities.

For example, consider the case arising from excitations of the two valence electrons in the valence orbitals $4p_{1/2}$ or $4p_{3/2}$. There are 5 possible excitation channels responding to the electric-type dipole excitation (by a $E_{J=1}$ operator):

TABLE I. The binding energies (in eV) of the atomic germanium orbits from the present MCDF calculations. The experimental data are the edge energies extracted from photoabsorption data of germanium solids.

Label		MCDF	Exp. ^a
Subshell	Orbital		
N_{III}	$4p_{1/2}$	7.8	
N_{II}	$4p_{3/2}$	8.0	
N_I	$4s_{1/2}$	15.4	
M_V	$3d_{5/2}$	43.1	29.3
M_{IV}	$3d_{3/2}$	43.8	29.9
M_{III}	$3p_{3/2}$	140.1	120.8
M_{II}	$3p_{1/2}$	144.8	124.9
M_I	$3s_{1/2}$	201.5	180.1
L_{III}	$3p_{3/2}$	1255.6	1217.0
L_{II}	$3p_{1/2}$	1287.9	1248.1
L_I	$2s_{1/2}$	1454.4	1414.6
K	$1s_{1/2}$	11185.5	11103.1

^aFrom Ref. [37].

TABLE II. Configuration weights of the germanium atom in its ground state ($J^\pi = 0^+$) from the present MCDF calculations.

Valence Configuration	Configuration Weight	Percentage
$4p_{1/2}^2$	0.84939	72.15%
$4p_{3/2}^2$	0.52776	27.85 %

$$4p_{1/2} \rightarrow \epsilon s_{1/2},$$

$$4p_{1/2} \rightarrow \epsilon d_{3/2},$$

$$4p_{3/2} \rightarrow \epsilon s_{1/2},$$

$$4p_{3/2} \rightarrow \epsilon d_{3/2},$$

$$4p_{3/2} \rightarrow \epsilon d_{5/2}.$$

Besides the above valence-excitation channels, the 10 inner core orbitals give rise to additional 24 channels. In total, when one considers all possible excitations from all orbitals, there are 29 excitation channels to be taken into account in the electric-type dipole excitation. These 29 interacting jj -coupled channels are all included in our MCRRPA framework to account for the final ionic-state electron correlations. The corresponding MCRRPA equations comprise a system of coupled differential equations up to 29 channels with 116 unknown radial functions to be numerically solved in a self-consistent manner.

To obtain the total photoabsorption cross section, all electric-type (E_J) and magnetic-type (M_J) multipole excitations which contribute to the on-shell transverse response function, $R_{11+22}^{(\gamma)}(q^2 = 0)$, are summed. For photons with energy $T \lesssim 10$ keV, it is found that high-order multipole transition probabilities decrease rapidly in an exponential mode. We choose the cut-off value J_{cut} in the multipole expansion by the following recursive procedure: We first sum over the multipole transition probabilities up to a definite polarity order (which should be high enough so the rapidly-decreasing pattern starts to show), and extrapolate the corrections from succeeding higher multipoles by a proper exponential form. Then J_{cut} is fixed once the contributions from $\sum_{J>J_{\text{cut}}}$ is estimated, by the exponential law, to be below 1% of the total from $\sum_{J \leq J_{\text{cut}}}$.

In Fig. 1(a), the photoabsorption cross sections from the MCRRPA method and experimental data are shown for incident photon energies ranging from 10 eV to 10 keV. The MCRRPA results agree very well with experiments for photon energies larger than 80 eV, with errors uniformly below the 5% level. The discrepancy below 80 eV is relatively large and we believe it is due to the fact that the experimental data were taken from solid-phase Ge targets, whose wave functions and orbital binding energies, in particular for outer-shell electrons, are affected by nearby atoms and therefore different from the ones of a single atom. As shown by Table I and Fig. 1(a), the solid effects are especially significant for the $3d$ orbitals. On the other hand, the inner-shell electrons are less affected by crystal structure; as a result, our calculation well-reproduces the data of photon energies $T \geq 100$ eV, where cross sections are dominated by ionization of inner-shell electrons. To estimate the degree to which our MCRRPA results will be affected by the solid effects in the $T \geq 100$ eV

region, we carried out a parallel calculation in which the theoretical ionization thresholds are artificially aligned with the experimental ones. The results, plotted in Fig. 1(b), show that the deviations from experimental data are still kept below the 10% level. Therefore, we estimate the theoretical uncertainty due to the solid effects to be $\lesssim 10\%$ in the $T \geq 100$ eV region.

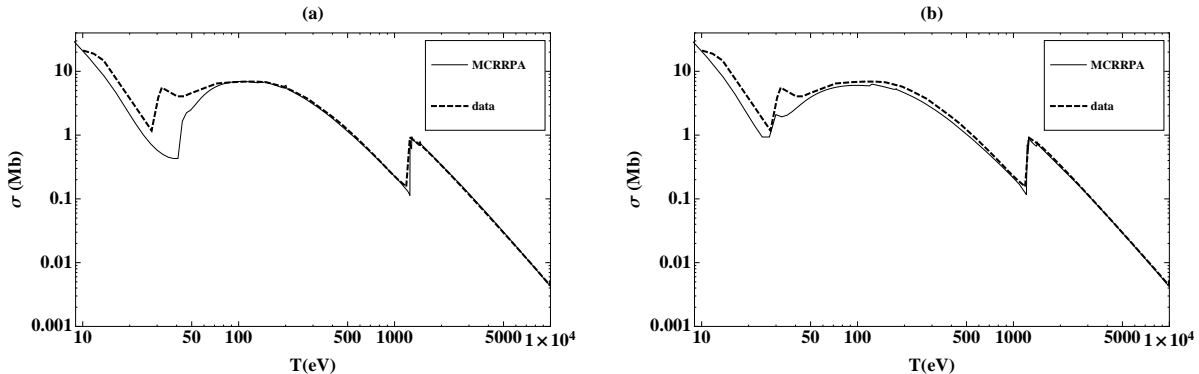


FIG. 1. Photoabsorption cross sections of Ge. The data are taken from Ref. [37]. The MCCRPA line in panel (a) shows our numerical results; the one in panel (b) is obtained by forcing all shell energies aligned to the experimental edge energies.

Summing up this section, we demonstrate that our MCCRPA approach is capable of giving a good description of a germanium atom and its photoabsorption process with photon energy larger than 100 eV. In other words, the many-body wave functions, single particle basis states, and relevant transition matrix elements thus obtained should be good approximations to the exact answers. In the next section, we shall apply this approach to germanium ionization by neutrinos.

IV. IONIZATION OF GERMANIUM BY NEUTRINOS

As shown in Eqs. (14,17,20), ionization of germanium by neutrinos depends on various atomic response functions R 's, which need explicit many-body calculations. The only differences in calculating the response functions for this case from the ones for photoionization are (i) different atomic current operators are involved, and (ii) different kinematics are probed (the former are mostly off-shell, while the latter are purely on-shell). Therefore, it is straightforward to treat the problem in the MCCRPA framework simply by taking

more types of multipole operators and their off-shellness into account. Both aspects are not expected to generate additional complexity or problems in many-body physics, therefore, one can take similar confidence on MRRPA in this case as what has been acquired in the photoabsorption case with $T \geq 100$ eV.

Because q^2 in a t -channel scattering process is space-like, i.e., $q^2 < 0$ or $T^2 < |\vec{q}|^2$, an off-shell current operator typically yields a multipole expansion which converges more slowly than its on-shell counterpart. Here we use an example to demonstrate a multipole expansion scheme is still valid and effective for the cases we are interested. Consider an incident neutrino with 1 MeV energy (a typical value for reactor antineutrinos) and depositing 1 keV energy to the detector through the charge-type multipole operators \hat{C}_{JM} in weak, magnetic moment, or millicharge interactions. The contributions of \hat{C}_{JM} to the differential cross sections $d\sigma/dT$ in these three cases are plotted in Fig. 2(a), (b), and (c), respectively. All these plots feature exponential decay behaviors with increasing multipolarity J , and they are fitted to be proportional to $e^{-0.15J}$, $e^{-0.14J}$, and $e^{-0.10J}$, respectively. Therefore, we can apply the same cutoff procedure mentioned in the last section in multipole expansions and control the higher-multipole uncertainty at the 1% level. For the entire kinematics considered in this work, it is found that the cutoff values J_{cut} are no more than 50 – 60.

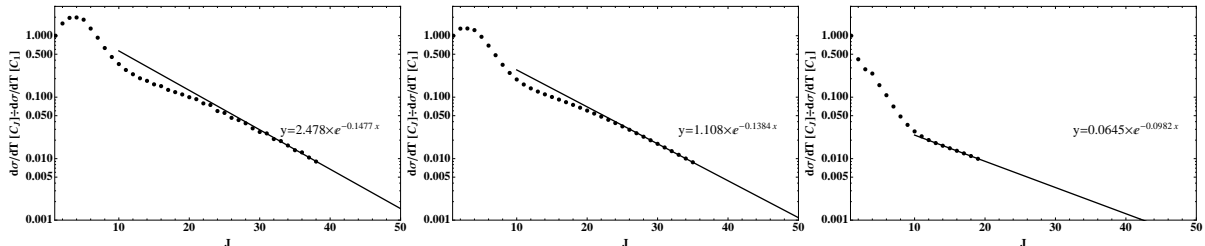


FIG. 2. Normalized contributions from the series of charge multipole operators C_J 's to differential cross sections for (a) weak interaction, (b) magnetic moment interaction, and (c) millicharge interaction. The incident neutrino has 1 MeV energy and deposits 1 keV energy.

A. Results and Discussion

In this section, we present our calculated differential cross sections for germanium ionization with two representative incident neutrino energies: (a) $E_\nu = 1$ MeV and (b) $E_\nu = 10$ keV. The former case is typical for reactor antineutrinos, while the latter case gives an

example of very low energy neutrinos, e.g., ones from tritium β decay.

1. Weak Interaction

The differential cross sections due to the weak interaction, i.e., Eq. (14), are given in Fig. 3 (see also Fig. 2 in Ref. [17]). As shown in panel (a), our MCRSPA calculation and the conventional FEA scheme gradually converge when the energy transfer is larger than 1 keV. On the other hand, below $T = 1$ keV, FEA starts to overestimate the differential cross sections. In other words, we found the atomic binding effect suppress the weak scattering cross sections at low energies in comparison to the free scattering picture. This conclusion is consistent with previous explicit many-body calculations [18–21].

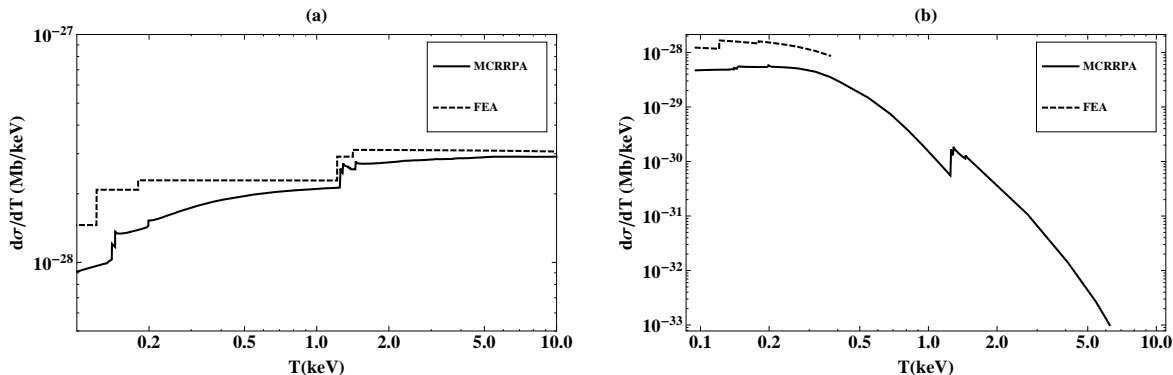


FIG. 3. Differential cross sections for germanium ionization by neutrino weak interaction with neutrino incident energies (a) $E_\nu = 1$ MeV and (b) $E_\nu = 10$ keV. (See also Fig. 2 in Ref. [17])

In very low energy neutrino scattering, the FEA scheme has another severe problem that comes with its specific kinematic constrain: $q^2 = -2m_e T$. This leads to a maximum energy transfer $T_{\max} \approx 0.38$ keV for a 10-keV neutrino beam—as shown by the sharp cutoff for the FEA curve in panel (b); while there is no such cutoff expected in a neutrino–atom ionization process. Experiments with good energy resolution should be able to discern this difference.

2. Magnetic Moment Interaction

The differential cross sections due to the interaction with $\kappa_\nu^{(\text{eff})}$, i.e., Eq. (20), are given in Fig. 4 (see also Fig. 2 in Ref. [17]). The comparison of the MCRSPA and FEA results shows very similar features as the case of weak scattering: FEA overestimates in the $T \lesssim 1$ keV

region and gradually converges to MCRRPA for $T \gtrsim 1$ keV, and our conclusion in this case is also consistent with previous explicit many-body calculations [18–21].

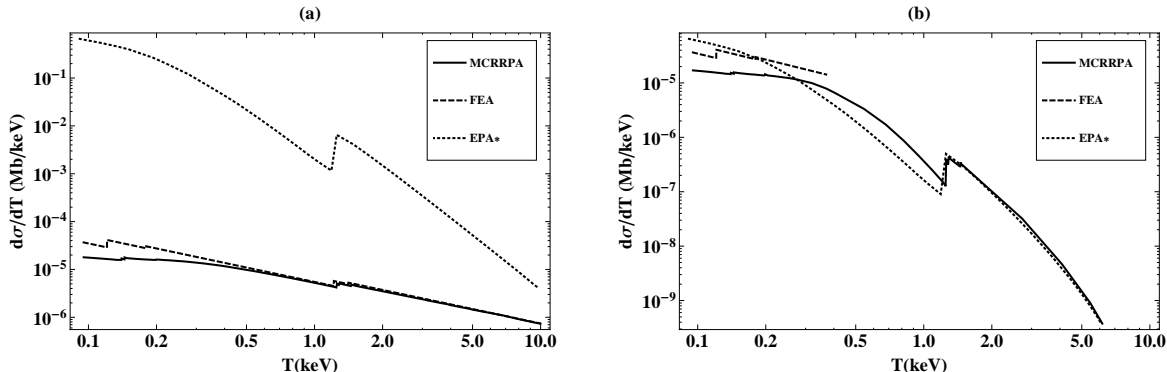


FIG. 4. Differential cross sections for germanium ionization by neutrino magnetic moment interaction with neutrino incident energies (a) $E_\nu = 1$ MeV and (b) $E_\nu = 10$ keV, in units of $\kappa_\nu^{(\text{eff})2}$. (See also Fig. 2 in Ref. [17])

As there have been quite extensive recent discussions about the role of atomic structure in scattering by neutrino magnetic moments, we try to clarify the confusion which is caused by the applicabilities of various approximation schemes:

1. EPA: It was first claimed in Ref. [3] that atomic structure can greatly enhance the sensitivity to $\kappa_\nu^{(\text{eff})}$ by orders of magnitude than the FEA prediction in the $T < 1$ keV region for germanium. However, later works inspired by this, using various approaches, all came to the opposite conclusion [17, 22–24]. The source of the huge overestimation in Ref. [3]: the use of an unconventional EPA scheme, was pointed out in Ref. [31] by considering a simple case of hydrogen atoms. Applying the same scheme to germanium, the results are shown by the EPA* curves in Fig. 4. In panel (a), one clearly sees the orders-of-magnitude enhancement that EPA* predicts. On the other hand, in panel (b), EPA* does agree well with MCRRPA for $T > 1$ keV. This is consistent with the feature pointed out in Ref. [31]: When incident neutrino energy (in this case, 10 keV) falls below the scale of atomic binding momentum (in this case, 35 keV for the most important $3p$ shell), the EPA* works incidentally.
2. The Voloshin sum rules: Quantum-mechanical sum rules for neutrino weak and magnetic-moment scattering were derived by Voloshin [22] and refined in later works [23,

24]. Using several justified assumptions, the sum rules concluded that treating atomic electrons as free particles be a good approximation. One important step in these sum rules is extending the integration over q^2 (equivalent to integration over the neutrino scattering angle θ for a fixed T) from the physical range $[T^2, 4E_\nu^2]$ to $[0, \infty)$. In this sense, the sum-rule results, or equivalently the FEA results, can be interpreted as upper limits for realistic $d\sigma/dT$, and this is consistent with our MCRRPA curves being under the FEA ones in Figs. 3 and 4. However, the larger discrepancy between realistic calculations and FEA at sub-keV energies seems to be in contradiction with the sum-rule-FEA argument: With low T , only outer-shell electrons are ionized, so the sum rules should work even better, not worse, since these electrons are less bound, or closer to be free electrons. The main reason, as pointed out in Ref. [16], is the missing of two-electron correlation in the sum rule derivation, which plays a more important role at low energies.

3. Millicharge Interaction

The differential cross sections due to the interaction quadratic in q_ν , i.e., Eq. (17), are given in Fig. 5. While the linear term due to the EM-weak interference can be calculated straightforwardly, it can be safely ignored at the current and projected sensitivity levels of direct experiments with $q_\nu \sim 10^{-12} - 10^{-13}$.

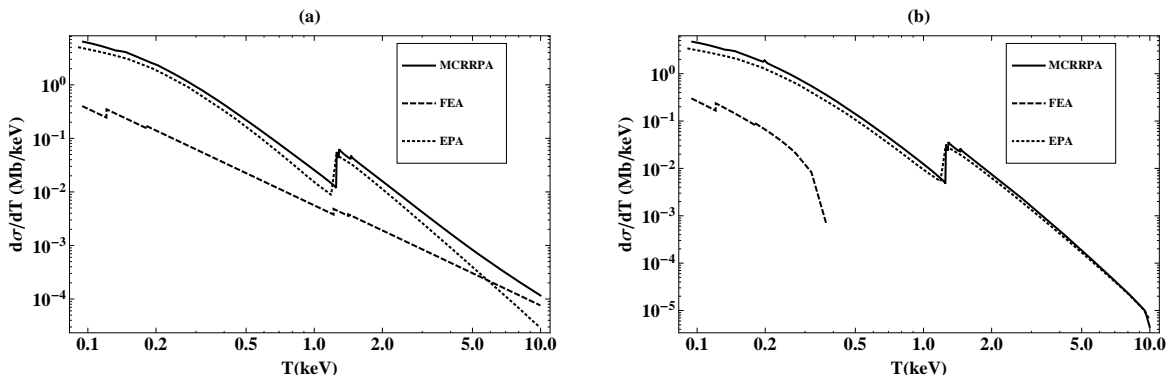


FIG. 5. Differential cross sections for germanium ionization by neutrino millicharge interaction with neutrino incident energies (a) $E_\nu = 1$ MeV and (b) $E_\nu = 10$ keV, in units of q_ν^2 .

Unlike the previous two cases that FEA works well for neutrino weak and magnetic

moment scattering with big enough incident energy E_ν and energy deposition T , it underestimates the millicharge scattering cross sections, in particular in the most interested sub-keV region of T . Instead, it is EPA that works much better in this case. The main reason, as pointed out in Ref. [31], is due to the kinematic factor $1/q^2$ that goes along the transverse response function $R_{11+22}^{(\gamma)}$ in Eq. (17). This factor weights more the forward scattering region with $q^2 \rightarrow 0$, where photons behave like real particles. For the same reason one can see that the FEA constraint: $q^2 = -2m_e T$ deviates substantially from the true kinematics of this scattering process.

Because of the same $1/q^2$ factor, we also note that the differential cross section contains a logarithmic term $\log(E_\nu/m_\nu)$, which diverges at the limit of massless neutrinos [4]. While it is known that neutrinos are not massless, their masses have not been determined precisely yet. Instead of using the current upper limit $m_{\nu_e} < 2 \text{ eV}$ as the cutoff value in this logarithm to present our results in this paper, we adopt the Debye length of germanium solid: $0.68 \mu\text{m}$ which characterizes the scale of screen Coulomb interaction and acts like a 0.29 eV mass cutoff (a value also similar to the projected sensitivity on m_{ν_e} by the KATRIN experiment). The uncertainty in cross sections due to this one-order-of-magnitude difference in the mass cutoff is about 20%.

4. Charge Radius Interaction

The differential cross sections due to the interaction with $\langle \mathbf{x}_\nu^2 \rangle^{(\text{eff})}$, i.e., by taking $d\sigma^{(\text{h.c.})}/dT - d\sigma^{(w)}/dT$ with $\mathbf{q}_\nu = 0$ in Eq. (16), are given in Fig. 6. Since the charge radius interaction takes the same contact form as the weak interaction, it is natural to expect the failure of the EPA scheme, so not shown in the figure. The main difference between the charge radius and weak interactions is that the former depends on the atomic vector-current response, while the latter on the atomic vector-minus-axial-vector-current (V-A) response. However, as can be seen from the comparison of Figs. 6 and 3, both differential cross sections share very similar T -dependence. The differences between the MCRRPA and FEA results are also similar to the case of weak scattering.

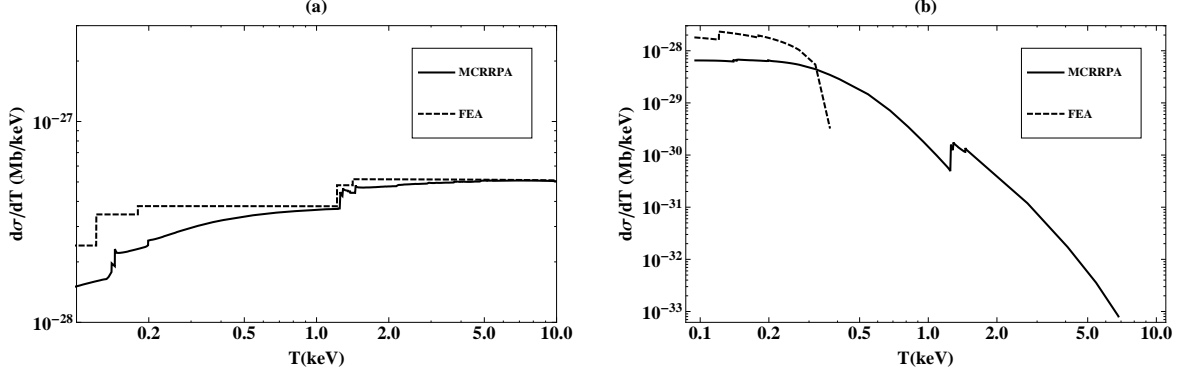


FIG. 6. Differential cross sections for germanium ionization by neutrino charge radius interaction with neutrino incident energies (a) $E_\nu = 1$ MeV and (b) $E_\nu = 10$ keV, in units of $2c_V\rho + \rho^2$ and $\rho \equiv \frac{\sqrt{2}\pi}{3} \frac{\alpha}{G_F} \langle \mathbb{r}_\nu^2 \rangle^{(\text{eff})}$.

B. Reactor Antineutrinos

Existing data from reactor neutrino experiments using germanium ionization detectors [5–8] provide excellent platform to investigate the atomic ionization effects induced by neutrino electromagnetic interactions. The sensitivities depend on the detectable threshold of the differential cross section, as well as the neutrino flux but are mostly independent to the neutrino energy. Therefore, the enormous $\bar{\nu}_e$ flux (order of $10^{13} \text{ cm}^{-2} \text{ s}^{-1}$, at a typical distance of 20 m from the reactor core) at the MeV-range energy from nuclear power reactors is a well-suited source. The germanium detectors, with their excellent energy resolution and sub-keV threshold, are ideal as means of studying these effects. The experimental features as peaks or edges at the definite K - and L -X-rays energies as well as with predictable intensity ratios provide potential smoking-gun signatures of these effects [3, 4].

Denoting the reactor $\bar{\nu}_e$ spectrum by $\phi(E_\nu)$, the measured differential spectra $\langle d\sigma/dT \rangle$ is related to the theoretical formulae of Eqs. 14, 17 and 20, via:

$$\left\langle \frac{d\sigma}{dT} \right\rangle = \frac{\int dE_\nu \phi(E_\nu) \frac{d\sigma}{dT}(E_\nu)}{\int dE_\nu \phi(E_\nu)}. \quad (47)$$

The measurable spectra due to weak interactions, neutrino magnetic moments at $\kappa_\nu^{(\text{eff})} = 10^{-11} \mu_B$, milli-charges at $q_\nu = 10^{-12} e$ and charge radius at $\langle \mathbb{r}_\nu^2 \rangle^{(\text{eff})} = [6 \times 10^{-3} \text{ fm}]^2$ at a reactor $\bar{\nu}_e$ flux of $10^{13} \text{ cm}^{-2} \text{ s}^{-1}$ are depicted in Fig. 7. These are compared with most sensitive data set from the TEXONO [5, 6] and GEMMA [7, 8] experiments and the corresponding

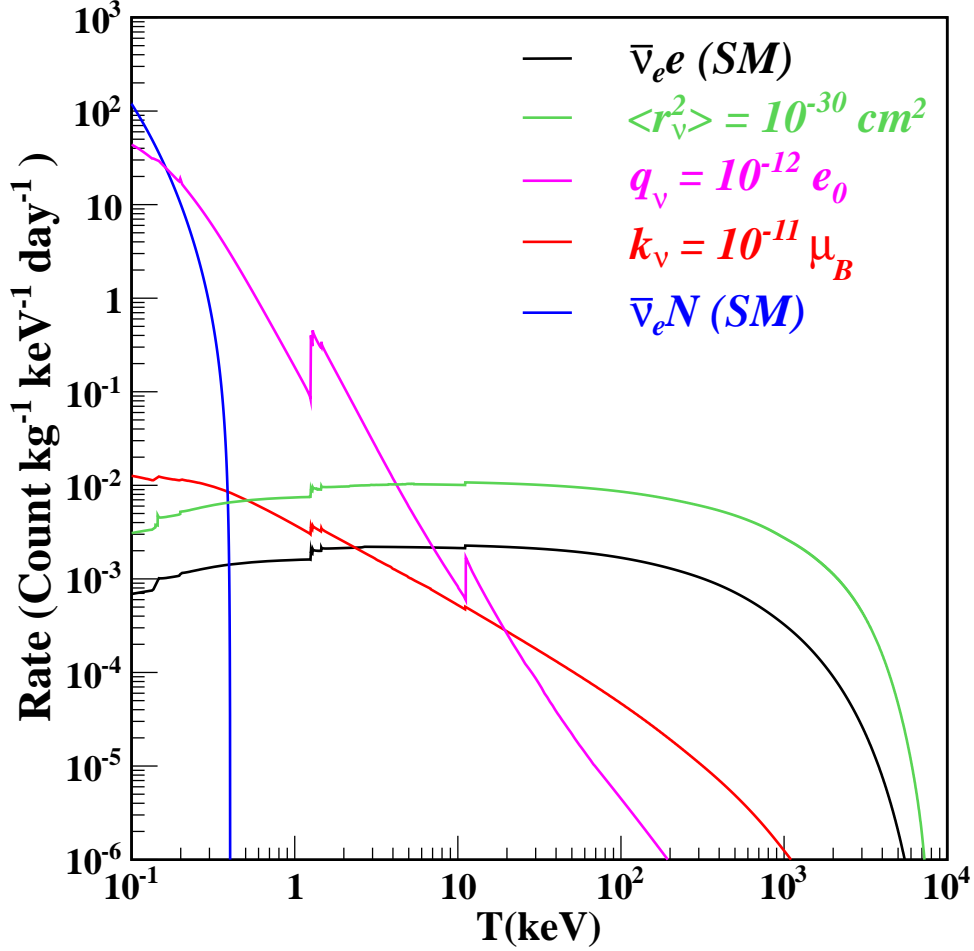


FIG. 7. Expected measurable spectra with Ge on the various neutrino electromagnetic effects from reactor neutrinos ($\bar{\nu}_e$) at a flux of $10^{13} \text{ cm}^{-2} \text{ s}^{-1}$. The spectra from SM weak processes involving the electrons ($\bar{\nu}_e e$) and the nucleus ($\bar{\nu}_e N$) are also included for comparisons.

limits at 90% CL are listed in Table III. Standard algorithms were adopted to provide best-fit and confidence intervals to the data (see, for example, the Statistics Section of Ref. [2]). Also shown are the potential sensitivities of a realistic next-generation measurements using Ge with sensitivities as low as 100 eV and at a background level of 1 count/kg-keV-day.

Both Fig. 7 and Table III confirm the merits of detectors with low-threshold and good energy resolution in the studies of $\kappa_\nu^{(\text{eff})}$ and q_ν , where the $d\sigma/dT$ formulae are enhanced as $T \rightarrow 0$. For $\langle r_\nu^2 \rangle^{(\text{eff})}$, detectors with larger mass like CsI(Tl) [9] making measurements at the MeV energy range to benefit from the better signal-to-background ratios would provide better sensitivities. .

Data Set	Reactor- $\bar{\nu}_e$		Data Strength		Analysis		Bounds at 90% CL		
	Flux ($\times 10^{13}$ cm $^{-2}$ s $^{-1}$)		Reactor ON/OFF (kg-days)	Threshold (keV)	$\kappa_{\bar{\nu}_e}^{(\text{eff})}$ ($\times 10^{-11}$ μB)	$q_{\bar{\nu}_e}$ ($\times 10^{-12}$)	$\langle \tau_{\bar{\nu}_e}^2 \rangle^{(\text{eff})}$ ($\times 10^{-30}$ cm 2)		
TEXONO 187 kg CsI [9]	0.64		29882.0/7369.0	3000	< 22.0	< 170	< 0.033		
TEXONO 1 kg Ge [5, 6]	0.64		570.7/127.8	12	< 7.4	< 8.8	< 1.40		
GEMMA 1.5 kg Ge [7, 8]	2.7		1133.4/280.4	2.8	< 2.9	< 1.1	< 0.80		
TEXONO Point-Contact Ge [4, 17]	0.64		124.2/70.3	0.3	< 26.0	< 2.1	< 3.20		
Projected Point-Contact Ge	2.7		800/200	0.1	< 1.7	< 0.06	< 0.74		
Sensitivity at 1% of SM	—		—	—	~ 0.023	~ 0.0004	~ 0.0014		

TABLE III. Summary of experimental limits at 90% CL on the various neutrino electromagnetic parameters studied in this work using selected reactor neutrino data. The projected sensitivities of measurements at the specified realistically experimental parameters are also shown. The last row illustrates the effective lower bounds to the sensitivities when a 1% measurement of the SM cross-section could be achieved, at threshold of 0.1 keV for $\kappa_{\bar{\nu}_e}^{(\text{eff})}$ and $q_{\bar{\nu}_e}$, and 3 MeV for $\langle \tau_{\bar{\nu}_e}^2 \rangle^{(\text{eff})}$, respectively.

C. Neutrinos of Tritium β Decay

The possibility of using the very low energy β neutrinos from tritium decay to constrain neutrino magnetic moments was discussed in Refs. [21, 25, 26]. In Fig. 8, we compare the convoluted differential cross sections calculated by our MCRRPA approach, Ref. [21], and the FEA scheme.

As shown by the figure, below $T < 1$ keV, FEA predicts larger cross sections for both neutrino weak and magnetic moment scattering than the two realistic many-body calculations. This echoes our previous argument that the Voloshin sum rule and FEA only poses an upper limit on cross sections, and the binding of an electron is not the only factor that determines whether FEA can be a good approximation or not. For $T > 0.9$ keV and $T > 0.5$ keV, FEA predictions drop quickly below the realistic calculations for weak and magnetic moment scattering, respectively. This is mainly because the maximum energy transfer allowed by FEA: $T_{\max} = 1.2$ keV (Q value for tritium β decay is 18.6 keV) heavily restricts the allowed final-state phase space for scattering.

While our MCRRPA approach agrees with the previous many-body calculations [21] in the $T > 0.9$ keV and $T > 0.5$ keV regions for weak and magnetic moment scattering, respectively; our results are comparatively smaller at lower T . This discrepancy is mostly related to the treatments in atomic many-body physics: (i) Ref. [21] adopted the same framework as Refs. [18–20] by using the relativistic Dirac-Hartree-Fock method with a local exchange potential to solve the atomic ground-state structure, while we used the exact non-local Fock potential. (ii) The local exchange potential used by Ref. [21] is adapted from Ref. [38]. This local exchange potential is designed to describe the ground-state structure of several metals (with $Z < 50$) in the framework of density functional theory (DFT), therefore, it is not a surprise that it fits better the M -shell single particle energies of germanium crystal than our atomic calculations, because solid effects have been accounted for to some extent. (iii) It is known to be challenging to extend DFT to excited states (such as the ionization states which are relevant here); it is not clear how well the simplified mean-field scheme used by Ref. [21] can reproduce the photoabsorption data, say for $T > 100$ eV—which we take as a very important benchmark for the computation of transition matrix elements.

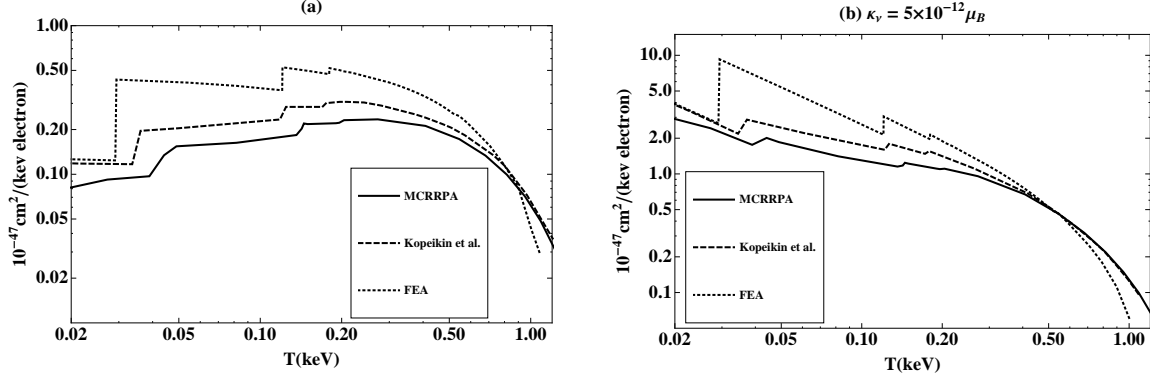


FIG. 8. Differential cross sections of germanium ionization by neutrinos of tritium β decay through (a) weak and (b) neutrino magnetic moment interaction assuming $\kappa_\nu^{(\text{eff})} = 5 \times 10^{-12} \mu_B$.

V. SUMMARY AND PROSPECTS

In this paper, we show that the multiconfiguration relativistic random phase approximation provides a good description for the structure of germanium atoms and the photoabsorption data of germanium solid at photon energy $\gtrsim 80$ eV. These benchmark calculations justify a good understanding of how germanium detectors respond to neutrinos, through weak and possible electromagnetic interactions, with a threshold as low as 100 eV.

After taking atomic ionization effects into account, existing reactor neutrino data with germanium detectors [7, 8] provide the most stringent direct experimental limits on neutrino millicharge and magnetic moments: $1.1 \times 10^{-12} e$ and $2.9 \times 10^{-11} \mu_B$ at 90% confidence level, respectively. Future experiments with 100 eV threshold can target at the $10^{-14} e$ and $10^{-12} \mu_B$ sensitivity range. In particular, there is substantial enhancement of the millicharge-induced cross section at low energy, providing smoking-gun signatures for positive signals. Charge-radius-induced interactions, on the other hand, do not have enhancement at low energy, such that the best sensitivities are obtained in experiment [9] with larger detector mass operating at the MeV energy range where the signal-to-background ratio is much more favorable.

The approach explored in this article as well as adopted by current laboratory experiments and astrophysics studies rely on searching possible anomalous effects relative to those produced by SM electroweak processes. It would therefore be experimentally difficult to probe non-standard effects less than, for example, 1% that of SM. There are certain fundamental (limited by physics rather than technology) lower bounds where such laboratory limits and astrophysics constraints can reach, as illustrated in Table III. This limitation can

be evaded, at least *conceptually*, by the analog of "appearance" experiments with the studies of detector channels where the SM background vanishes. For instance, in the case of Majorana neutrinos with transition magnetic moments, one can look for signatures of final-state neutrinos with a different flavor in a pure and intense neutrino beam which passes through a dense medium or an intense magnetic field. While there is no fundamental constraint to the lower reach of the sensitivities, realistic experiments are still many order-of-magnitude less sensitive than the reactor neutrino bounds [39, 40].

ACKNOWLEDGMENTS

We acknowledge the support from the NSC/MOST of ROC under Grant Nos. 102-2112-M-002-013-MY3 (JWC, CLW, CPW), 102-2112-M-259-005 and 103-2112-M-259-003 (CPL); the CTS and CASTS of NTU (JWC, CLW, CPW).

I. MULTIPOLE EXPANSION

First we set up the coordinate system so that the 3-momentum transfer by neutrinos is along the z -axis, i.e., the Cartesian unit vector $\hat{e}_3 = \vec{q}/|\vec{q}|$. The transformation between the unit vectors in the spherical ($\hat{e}^{\lambda=\pm 1,0}$) and Cartesian ($\hat{e}^{i=1,2,3}$) systems is then given by

$$\hat{e}^{\pm 1} = \mp \frac{1}{\sqrt{2}}(\hat{e}^1 \pm i\hat{e}^2), \quad \hat{e}^0 = \hat{e}^3. \quad (1)$$

The spherical component of a vector \vec{V} , denoted by λ ,³ is

$$V^\lambda = \hat{e}^\lambda \cdot \vec{V}. \quad (2)$$

According to Eq. (43), the perturbing field that gives rise to atomic ionization by neutrino electromagnetic interactions takes the form

$$\begin{aligned} \langle \Psi_f | v_+^{(\gamma)} | \Psi_i \rangle &= \frac{4\pi\alpha}{q^2} \left\{ j_0^{(\gamma)} \left\langle \Psi_f \left| \int d^3x e^{i\vec{q}\cdot\vec{x}} \hat{\mathcal{J}}^0(\vec{x}) \right| \Psi_i \right\rangle \right. \\ &\quad \left. + \sum_{\lambda=\pm 1,0} (-1)^\lambda j_\lambda^{(\gamma)} \left\langle \Psi_f \left| \int d^3x e^{i\vec{q}\cdot\vec{x}} \hat{\epsilon}^{-\lambda} \cdot \hat{\mathcal{J}}(\vec{x}) \right| \Psi_i \right\rangle \right\}. \quad (3) \end{aligned}$$

³ $V^{\lambda=0}$ should not to be confused with the time component of a Lorentz 4-vector.

Using the relations

$$e^{i\vec{q}\cdot\vec{x}} = \sum_{J=0}^{\infty} \sqrt{4\pi(2J+1)} i^J j_J(\kappa r) Y_J^0(\Omega_x), \quad (4)$$

$$e^{i\vec{q}\cdot\vec{x}} \hat{\epsilon}^0 = \frac{-i}{\kappa} \sum_{J=0}^{\infty} \sqrt{4\pi(2J+1)} i^J \vec{\nabla} [j_J(\kappa r) Y_J^0(\Omega_x)], \quad (5)$$

$$e^{i\vec{q}\cdot\vec{x}} \hat{\epsilon}^{\pm 1} = - \sum_{J \geq 1} \sqrt{2\pi(2J+1)} i^J \left\{ \frac{1}{\kappa} \vec{\nabla} \times [j_J(\kappa r) \mathcal{Y}_{JJ_1}^{\pm 1}(\Omega_x)] \pm j_J(\kappa r) \mathcal{Y}_{JJ_1}^{\pm 1}(\Omega_x) \right\}, \quad (6)$$

where $|\vec{q}| \equiv \kappa$, $|\vec{x}| \equiv r$, $j_J(\kappa r)$ is the spherical Bessel function of order J , $Y_J^M(\Omega_x)$ the spherical harmonics, and $\mathcal{Y}_{JJ_1}^M(\Omega_x)$ the vector spherical harmonics formed by adding $Y_l^m(\Omega_x)$ and $\hat{\epsilon}^\lambda$ to be an angular momentum eigenstate $|JM\rangle$:

$$\mathcal{Y}_{JJ_1}^M(\Omega_x) \equiv \sum_{m\lambda} \langle lm1\lambda | l1JM \rangle Y_l^m(\Omega_x) \hat{\epsilon}^\lambda, \quad (7)$$

the perturbing field is expanded as

$$\begin{aligned} \langle \Psi_f | v_+^{(\gamma)} | \Psi_i \rangle &= \frac{4\pi\alpha}{q^2} \left\{ \sum_{J=0}^{\infty} \sqrt{4\pi(2J+1)} i^J \left[j_0^{(\gamma)} \langle \hat{C}_{J0}(\kappa) \rangle - j_3^{(\gamma)} \langle \hat{L}_{J0}(\kappa) \rangle \right] \right. \\ &\quad \left. + \sum_{J \geq 1} \sqrt{2\pi(2J+1)} i^J \sum_{\lambda=\pm 1} j_\lambda^{(\gamma)} \left[\langle \hat{E}_{J-\lambda}(\kappa) \rangle - \lambda \langle \hat{M}_{J-\lambda}(\kappa) \rangle \right] \right\}. \quad (8) \end{aligned}$$

The various spherical multipole operators are defined by

$$\hat{C}_{JM}(\kappa) = \int d^3x [j_J(\kappa r) Y_{JM}] \hat{\mathcal{J}}^0(\vec{x}), \quad (9)$$

$$\hat{L}_{JM}(\kappa) = \frac{i}{\kappa} \int d^3x \vec{\nabla} [j_J(\kappa r) Y_{JM}(\Omega_x)] \cdot \hat{\mathcal{J}}(\vec{x}) \quad (10)$$

$$\hat{E}_{JM}(k) = \frac{1}{\kappa} \int d^3x \vec{\nabla} \times [j_J(\kappa r) \mathcal{Y}_{JJ_1}^M(\Omega_x)] \cdot \hat{\mathcal{J}}(\vec{x}) \quad (11)$$

$$\hat{M}_{JM}(k) = \int d^3x [j_J(\kappa r) \mathcal{Y}_{JJ_1}^M(\Omega_x)] \cdot \hat{\mathcal{J}}(\vec{x}). \quad (12)$$

Each operator has its specific angular momentum and parity selections rules that restrict the possible initial-to-final-state transitions.

When dealing with weak interactions, the axial vector current operator $\hat{\mathcal{J}}_5(\vec{x})$ generates additional four types of multipole operators \hat{C}_{JM}^5 , \hat{L}_{JM}^5 , \hat{E}_{JM}^5 , and \hat{M}_{JM}^5 . They are obtained

simply by replacing the vector current operator $\hat{\mathcal{J}}(\vec{x})$ with $\hat{\mathcal{J}}_5(\vec{x})$ in the above definitions.

- [1] C. Giunti and A. Studenikin, (2014), [arXiv:1403.6344 \[hep-ph\]](#); C. Brogini, C. Giunti, and A. Studenikin, *Adv. High Energy Phys.* **2012**, 459526 (2012); H. T. Wong and H. B. Li, *Mod. Phys. Lett. A* **20**, 1103 (2005).
- [2] K. Olive *et al.* (Particle Data Group), *Chin. Phys. C* **38**, 090001 (2014).
- [3] H. T. Wong, H.-B. Li, and S.-T. Lin, *Phys. Rev. Lett.* **105**, 061801 (2010), erratum: [arXiv:1001.2074v3](#).
- [4] J.-W. Chen, H.-C. Chi, H.-B. Li, C.-P. Liu, L. Singh, *et al.*, (2014), [arXiv:1405.7168 \[hep-ph\]](#).
- [5] H. B. Li *et al.*, *Phys. Rev. Lett.* **90**, 131802 (2003).
- [6] H. T. Wong *et al.*, *Phys. Rev. D* **75**, 012001 (2007).
- [7] A. Beda *et al.*, *Adv. High Energy Phys.* **2012**, 350150 (2012).
- [8] A. G. Beda *et al.*, *Phys. Part. Nucl. Lett.* **10**, 139 (2013).
- [9] M. Deniz *et al.* (TEXONO Collaboration), *Phys. Rev. D* **82**, 033004 (2010), [arXiv:1006.1947 \[hep-ph\]](#).
- [10] S. Gninenko, N. Krasnikov, and A. Rubbia, *Phys. Rev. D* **75**, 075014 (2007), [arXiv:hep-ph/0612203 \[hep-ph\]](#).
- [11] A. Studenikin, (2013), [arXiv:1302.1168 \[hep-ph\]](#).
- [12] S. T. Lin *et al.*, *Phys. Rev. D* **79**, 061101 (2009).
- [13] H. B. Li *et al.*, *Phys. Rev. Lett.* **110**, 261301 (2013).
- [14] W. Zhao *et al.*, *Phys. Rev. D* **88**, 052004 (2013).
- [15] R. Agnese *et al.* (SuperCDMS Collaboration), *Phys. Rev. Lett.* **112**, 241302 (2014), [arXiv:1402.7137 \[hep-ex\]](#).
- [16] K. A. Kouzakov and A. I. Studenikin, (2014), [arXiv:1406.4999 \[hep-ph\]](#).
- [17] J.-W. Chen, H.-C. Chi, K.-N. Huang, C.-P. Liu, H.-T. Shiao, *et al.*, *Phys. Lett. B* **731**, 159 (2014), [arXiv:1311.5294 \[hep-ph\]](#).
- [18] S. Fayans, V. Y. Dobretsov, and A. Dobrotsvetov, *Phys. Lett. B* **291**, 1 (1992).
- [19] V. I. Kopeikin, L. A. Mikaelyan, V. V. Sinev, and S. A. Fayans, *Phys. At. Nucl.* **60**, 1859 (1997).
- [20] S. Fayans, L. Mikaelyan, and V. Sinev, *Phys. Atom. Nucl.* **64**, 1475 (2001).

- [21] V. Kopeikin, L. Mikaelian, and V. Sinev, *Phys. Atom. Nucl.* **66**, 707 (2003).
- [22] M. B. Voloshin, *Phys. Rev. Lett.* **105**, 201801 (2010), erratum: *ibid.* **106**, 059901 (2011).
- [23] K. A. Kouzakov and A. I. Studenikin, *Phys. Lett. B* **696**, 252 (2011).
- [24] K. A. Kouzakov, A. I. Studenikin, and M. B. Voloshin, *Phys. Rev. D* **83**, 113001 (2011).
- [25] Y. Giomataris and J. D. Vergados, *Nucl. Instrum. Meth. A* **530**, 330 (2004).
- [26] G. C. McLaughlin and C. Volpe, *Phys. Lett. B* **591**, 229 (2004).
- [27] M. J. Musolf and B. R. Holstein, *Phys. Rev. D* **43**, 2956 (1991).
- [28] C. F. von Weizsacker, *Z. Phys.* **88**, 612 (1934).
- [29] E. J. Williams, *Phys. Rev.* **45**, 729 (1934).
- [30] W. Greiner and J. Reinhardt, *Quantum Electrodynamics*, 4th ed. (Springer, 2009).
- [31] J.-W. Chen, C.-P. Liu, C.-F. Liu, and C.-L. Wu, *Phys. Rev. D* **88**, 033006 (2013).
- [32] K.-N. Huang, H.-C. Chi, and H.-S. Chou, *Chin. J. Phys.* **33**, 565 (1995).
- [33] K.-N. Huang and W. R. Johnson, *Phys. Rev. A* **25**, 634 (1982).
- [34] K.-N. Huang, *Phys. Rev. A* **26**, 734 (1982).
- [35] W. R. Johnson and K.-N. Huang, *Phys. Rev. Lett.* **48**, 315 (1982).
- [36] J. P. Desclaux, *Comp. Phys. Comm.* **9**, 31 (1975).
- [37] B. L. Henke, E. M. Gullikson, and J. C. Davis, *At. Data Nucl. Data Tables* **54**, 181 (1993).
- [38] V. L. Moruzzi, J. F. Janak, and A. R. Williams, *Calculated Electronic Properties of Metals* (Pergamon, Oxford, 1978).
- [39] M. Gonzalez-Garcia, F. Vannucci, and J. Castromonte, *Phys. Lett. B* **373**, 153 (1996), [arXiv:hep-ph/9510316](https://arxiv.org/abs/hep-ph/9510316) [hep-ph].
- [40] J. Frère, R. Nevzorov, and M. Vysotsky, *Phys. Lett. B* **394**, 127 (1997), [arXiv:hep-ph/9608266](https://arxiv.org/abs/hep-ph/9608266) [hep-ph].